Electrochemistry
The Electrochemical Society of Japan
Received: December 29, 2023
Accepted: February 18, 2024
Published online: February 22, 2024
Issued: April 1, 2024
https://doi.org/10.5796/electrochemistry.23-69166
https://doi.org/10.50892/data.electrochemistry.25255051
Article
Electrochemistry, 92(4), 043017 (2024)

The 69th special feature "Frontiers of Molten Salts and Ionic Liquids"

In-Situ Raman Spectroscopic Analysis of Factors Improving Discharge Rate Capability of Na-Ion Batteries with FSA-Based Ionic Liquids†

OPEN ACCESS

Yoshifumi ISHIO,§ Takayuki YAMAMOTO,*,§§ Koki MANABE, and Toshiyuki NOHIRA§§§

Institute of Advanced Energy, Kyoto University, Gokasho, Uji, Kyoto 611-0011, Japan

* *Corresponding author: yamamoto.takayuki.2w@kyoto-u.ac.jp*

ABSTRACT

Na-ion batteries (NIBs) with ionic liquid (IL) electrolytes are promising candidates for large-scale energy storage devices owing to the abundance of Na resources and the safety of ILs. In our previous study, we have demonstrated the improved rate capability of NIBs consisting of a hard carbon negative electrode, an $NaCrO_2$ positive electrode, and an FSA-based IL electrolyte (FSA = bis(fluorosulfonyl)-amide) by increasing the Na^+ ion concentration in the IL. However, this phenomenon is not consistent with the trend observed for the ionic conductivities of bulk ILs. In this study, to clarify the unexplained behavior particularly for electrolytes with high Na^+ concentrations, we performed in-situ Raman spectroscopic analysis in the vicinity of the electrode/electrolyte interface. The results of discharge rate capability tests indicated that a rate-determining step existed in the reaction at the positive electrode, where Na^+ insertion occurred during discharge. In-situ Raman spectroscopy for Na/$NaCrO_2$ half-cells using an IL electrolyte of low Na^+ concentration (∼1 mol dm^{-3}) revealed that the Na^+ ion concentration at the interface (inside the $NaCrO_2$ composite electrode) locally decreased as the discharging proceeded. In contrast, a high Na^+ concentration electrolyte (∼2.2 mol dm^{-3}) considerably suppressed the decrease in the Na^+ ion concentration at the interface. Therefore, the improved performance of the electrolyte with a high Na^+ concentration can be explained by the local Na^+ ion concentration near the electrode/electrolyte interface, rather than by the bulk properties of the IL electrolytes.

Keywords : Na-ion Battery, FSA-based Ionic Liquid, Raman Spectroscopy, In-situ Analysis

1. Introduction

To mitigate environmental issues such as global warming, it is imperative to transition from conventional fossil fuels to renewable energy.[1] Renewable energy sources such as solar photovoltaics depend on weather conditions and exhibit significant temporal fluctuations in the generated energy. Under these conditions, large-scale energy storage technologies have become indispensable. For example, pumped storage hydropower serves as a large-scale energy storage method. However, addressing short-term fluctuations in input and output is challenging. Consequently, there is demand for large-scale rechargeable batteries with excellent input and output characteristics.[2–4]

Li-ion batteries (LIBs) are widely used in compact electronic devices such as mobile phones and laptops because of their high energy density. Recently, they have been increasingly used as large-scale rechargeable batteries in hybrid vehicles and electric vehicles. However, two significant factors limit the application of LIBs in large-scale devices: the use of flammable electrolytes[5] and the reliance on scarce resources such as Li and Co.[6–8] One solution to these problems is the development of Na-ion batteries (NIBs) which utilize nonflammable and nonvolatile ionic liquids (ILs)[9–11] and the abundant resources of Na.[12,13]

Researchers have explored various active materials and electrolytes for NIBs,[14,15] and various groups, including ours, have developed IL electrolytes that meet both safety and performance requirements.[16–27] In the present study, an Na[FSA]–[C_3C_1pyrr][FSA] (FSA = bis(fluorosulfonyl)amide, C_3C_1pyrr = *N*-methyl-*N*-propylpyrrolidinium) IL was used as the NIB electrolyte. Notably, for the IL at x(Na[FSA]) = 0.20 (x(Na[FSA]): molar fraction of Na[FSA]), a high ionic conductivity of 15.6 mS cm^{-1} and a broad electrochemical window of approximately 5 V were confirmed at 353 K.[23] The drawbacks of NIBs, such as their lower energy densities compared with LIBs, are typically discussed with regard to the well-known redox potentials of alkali metals in aqueous solutions; that is, the standard redox potential of Na^+/Na in water is 0.3 V higher than that of Li^+/Li.[28] However, those potentials largely depend on the type of electrolytes. For instance, in M[FSA]–[C_3C_1pyrr][FSA] ILs (M = Li, Na; x(M[FSA]) = 0.20), the potential difference between Na^+/Na and Li^+/Li redox couples decreases to approximately 0.1 V ($E(Na^+/Na) \approx E(Li^+/Li) + 0.1$).[29] Thus, the use of IL electrolytes is a promising solution for mitigating the drawbacks of reduced energy density in NIBs.

Our group demonstrated the use of various active materials in the Na[FSA]–[C_3C_1pyrr][FSA] IL electrolyte.[23–25] Specifically, a practical Na-ion full cell comprising a hard carbon (HC) negative electrode and an $NaCrO_2$ positive electrode was fabricated, which exhibited energy densities of 125 Wh L^{-1} and 75 Wh kg^{-1} within the operating temperature range of 298–363 K.[26] Furthermore, an increase in the Na[FSA] composition of the electrolyte improves

†A part of this paper has been presented in 2023 Joint Symposium on Molten Salts (Presentation #P04).

§ECSJ Student Member
§§ECSJ Active Member
§§§ECSJ Fellow
T. Yamamoto orcid.org/0000-0003-3553-3272
T. Nohira orcid.org/0000-0002-4053-554X

the discharge rate capability.[30] However, the Na^+ conductivity of the bulk electrolyte decreases with increasing Na[FSA] composition.[21] The phenomenon of improved rate capability cannot be explained solely by the properties of the bulk electrolyte. Therefore, it is necessary to analyze the electrolyte in the vicinity of the electrode/electrolyte interface rather than in the bulk. In-situ Raman spectroscopy is a useful method for observing changes in electrolytes inside battery cells. In a previous study, in-situ Raman spectroscopy was employed to investigate the behavior of batteries using Li and Na electrolytes.[31] By utilizing the relationship between concentration changes and peak shifts in the Raman spectra, the diffusion properties of Na^+ and Li^+ were compared in solid polymer electrolytes, which revealed that solvation/desolvation of Na^+ by $TFSA^-$ (TFSA = bis(trifluoromethylsulfonyl)amide) during ionic transport is more difficult than the case of Li^+.

Concerning FSA-based ILs with imidazolium cations, the shift of FSA^- bands were observed by changing Na^+ ion concentration via ex-situ Raman spectroscopy,[22] which reflected the existence ratio of free FSA^- and the FSA^- complexed with Na^+ (bound FSA^-). Similar examinations were carried out for Li-based ILs containing $TFSA^-$ anions and $C_3C_1pyrr^+$ cations.[32,33] Thus, it is possible to detect the change of Na^+ ion concentration in the vicinity of electrode/electrolyte interface for the Na[FSA]–[C_3C_1pyrr][FSA] IL by in-situ Raman spectroscopy.

The present study confirmed that the positive electrode is a dominant factor affecting the discharge rate capability of HC/$NaCrO_2$ full cells. Then, the liquid structure of the electrolyte in the bulk and at the positive electrode/electrolyte interface was examined via ex-situ and in-situ Raman spectroscopy, revealing the factors contributing to the improved discharge rate capability.

2. Experimental

2.1 Materials preparation

Na[FSA] (Nippon Shokubai Co., Ltd., purity > 99 %) and [C_3C_1pyrr][FSA] (Kanto Chemical Co., Ltd.) were vacuum-dried at 353 K for 2 d and 333 K for 1 d before use. The Na[FSA]–[C_3C_1pyrr][FSA] IL electrolyte was prepared by mixing Na[FSA] and [C_3C_1pyrr][FSA] with a composition of x(Na[FSA]) = 0.10–0.50 (x(Na[FSA]): molar fraction of Na[FSA]) in an Ar-filled glovebox. The Na salt compositions of x(Na[FSA]) = 0.10, 0.20, 0.30, 0.40, and 0.50 correspond to the Na^+ molar concentrations (c_{Na^+}) of 0.45, 0.96, 1.5, 2.2, 3.0 mol dm^{-3} at 333 K, respectively.[21,30] To prepare the $NaCrO_2$ electrode slurry, $NaCrO_2$ powder, acetylene black (AB, Strem Chemicals, Inc.), and polyvinylidene fluoride (PVdF) in *N*-methyl-2-pyrrolidone (NMP) solution (Kishida Chemicals Co., Ltd.) were mixed. The weight ratio of $NaCrO_2$, AB, and PVdF is 85 : 10 : 5. Subsequently, NMP (FUJIFILM Wako Pure Chemicals Co., purity ≥ 99.0 %) was added to optimize the slurry properties. Similarly, for the HC electrodes, an aqueous slurry was prepared by mixing HC (Kuraray Co., Ltd.) and sodium carboxymethyl cellulose (CMC #2200, Daicel Miraizu Ltd.) at a weight ratio of 90 : 10. The prepared slurries were coated onto Al foil and vacuum-dried twice at 353 K for 1 d. The active material loading mass of the HC electrodes was within the range of 3.3–3.7 mg cm^{-2} for full cells. The active material loading mass of the $NaCrO_2$ electrodes was within the range of 10.2–11.3 mg cm^{-2} for full cells and 6.9–7.2 mg cm^{-2} for cells employed in in-situ Raman spectroscopy.

2.2 Electrochemical measurement and physical characterization

2.2.1 Half-cells and HC/$NaCrO_2$ full cells

Charge–discharge tests were performed using an electrochemical measurement apparatus (VSP, BioLogic Co. or 580-type battery cycler, Toyo Co.) and an airtight three-electrode cell (SB7, EC Frontier Co., Ltd.; see Fig. S1). Two sheets of glass fiber filter paper (Whatman GF/A) were used as the separator. Prior to the electrochemical measurements, the HC electrodes, $NaCrO_2$ electrodes, and separators were vacuum-impregnated with the electrolyte. Na metal (purity > 99.9 %; Sigma-Aldrich) was used as counter and reference electrodes for half-cell and as a reference electrode for full cell. A bench-top type temperature chamber (SU-222, ESPEC Corp.) was used to control the cell temperature. According to the results of the half-cell tests, the standard capacities of HC and $NaCrO_2$ were defined to be 275 and 100 mAh g^{-1} at 333 K, respectively (See Fig. S2). In the present study, a current density of 100 mA (g-$NaCrO_2$)$^{-1}$ was defined as 1 C rate. In the Na-ion full cells, the ratio of the standard capacities of HC and $NaCrO_2$ (N/P ratio: $R_{N/P} = Q_{HC}/Q_{NaCrO_2}$, Q is the quantity of electricity (mAh)) was controlled within the range of 0.88–0.90. The loading masses and N/P ratios are summarized in Table S1.

Initially, to stabilize the performance, all the full cells were operated at a rate of 0.2 C for three cycles with the limited charge capacity of 60 mAh (g-$NaCrO_2$)$^{-1}$ at 313 K. Then, the rate capability tests were conducted at 333 K within the voltage range of 1.5–3.4 V. The full-cell operation was also controlled by the cut-off potentials of negative and positive electrodes, i.e., 0.005 and 1.5 V (vs. Na^+/Na) for HC and 2.5 and 3.5 V (vs. Na^+/Na) for $NaCrO_2$. Each charging and discharging process was terminated when one of those conditions of the limit voltages and potentials was fulfilled. Discharging current density was varied from 0.2 C to 4 C rates, whereas charging current density was fixed at 0.2 C rate.

2.2.2 Ex-situ Raman spectroscopy of bulk electrolyte

The Raman spectra of Na[FSA]–[C_3C_1pyrr][FSA] (x(Na[FSA]) = 0–0.50) were obtained using a microscopic laser Raman spectrometer (Nanofinder 30, Tokyo Instruments Inc.). The measurements were conducted under Ar atmosphere at 333 K. An excitation laser with a wavelength of λ = 532 nm and an intensity of 15 mW was used.

2.2.3 In-situ Raman spectroscopy of Na/$NaCrO_2$ half-cells

In-situ Raman spectroscopic analysis of the Na/$NaCrO_2$ half-cells was performed using the same apparatus that was employed for ex-situ Raman spectroscopy. Specifically, a three-electrode cell for in-situ Raman spectroscopy (SB1300, EC Frontier Co., Ltd.) was constructed, as shown in Fig. 1, and Raman spectra were measured during charge–discharge tests using an electrochemical measurement device (ECstat302, EC Frontier Co., Ltd.). Electrodes and separators with a hole in the center were used for cell construction.

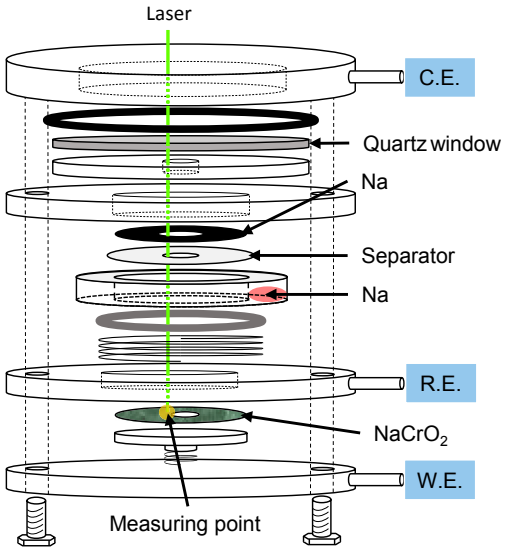

Figure 1. A schematic drawing of a three-electrode cell for in-situ Raman spectroscopy.

$NaCrO_2$ (outer diameter (OD) ϕ16 mm, inner diameter (ID) ϕ4 mm) was used for the working electrode, and Na metal (OD ϕ16 mm, ID ϕ6 mm) was used for the counter and reference electrodes. Two separators (OD ϕ18 mm, ID ϕ4.5 mm) were used per cell. The $NaCrO_2$ electrodes and separators were vacuum-impregnated with the electrolyte at 353 K for 1 d before use. During the charge–discharge tests, the cut-off potential was set as 2.50 and 3.45 V, and measurements were performed at 333 K. The cell was covered with a jacket heater connected to a temperature control unit. The charge current rate was 0.5 C rate and the discharge current rates were 0.5 C–4 C rates. An excitation laser with a wavelength of $\lambda =$ 532 nm and an intensity of 11 mW was used.

3. Results and Discussion

3.1 HC/$NaCrO_2$ full-cell performance

Figure 2 describes the typical charge–discharge curves of the HC/$NaCrO_2$ full cell using Na[FSA]–[C_3C_1pyrr][FSA] (x(Na[FSA]) = 0.20) IL electrolyte at 333 K. With an N/P ratio ($R_{N/P}$) of 0.90 for this cell, the ideal practical capacity ($C^{Id}_{Full\text{-}cell\ (NaCrO_2)}$) was calculated as 90 mAh (g-$NaCrO_2$)$^{-1}$ using Eq. 1 and the pre-confirmed $NaCrO_2$ standard capacity ($C^{Std}_{NaCrO_2} =$ 100 mAh g^{-1}).

$$C^{Id}_{Full\text{-}cell\ (NaCrO_2)} = C^{Std}_{NaCrO_2} \times R_{N/P}\ (R_{N/P} \leq 1) \qquad (1)$$

The full cell exhibited a reversible capacity of 87 mAh (g-$NaCrO_2$)$^{-1}$ at 0.2 C rate, which is close to the ideal practical capacity.

Figure 3 shows the discharge curves of HC/$NaCrO_2$ full cells with x(Na[FSA]) = 0.20 and 0.40 at various discharge rates from 0.2 C to 4 C and a constant charge rate of 0.2 C. As shown in Fig. 3a, the IL electrolyte at x(Na[FSA]) = 0.20 conferred a discharge capacity of 81 mAh (g-$NaCrO_2$)$^{-1}$ at 1 C rate, commensurate with 93 % of the capacity at the 0.5 C rate. However, the capacity drops to 51 mAh (g-$NaCrO_2$)$^{-1}$ at 2 C rate and further diminishes to 31 mAh (g-$NaCrO_2$)$^{-1}$ at 4 C rate.

In comparison, improved rate performance is confirmed when the Na salt fraction is increased to x(Na[FSA]) = 0.40 (Fig. 3b). A discharge capacity of 86 mAh (g-$NaCrO_2$)$^{-1}$ is maintained at 2 C rate, which is 1.7 times higher than the capacity at x(Na[FSA]) = 0.20. Comparing the discharge curves at the 2 C rate, minimal differences are observed in the HC potential profiles (black lines). However, the $NaCrO_2$ potential profiles (green lines) differ significantly. A rapid potential drop is observed at a capacity of 50 mAh (g-$NaCrO_2$)$^{-1}$ for the electrolyte of x(Na[FSA]) = 0.20, which can be attributed to the depletion of Na^+ ions in the $NaCrO_2$ composite electrode during the discharge (Na^+ insertion) process.

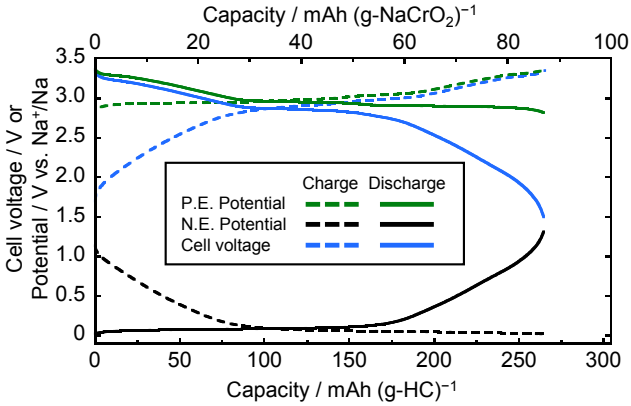

Figure 2. Charge–discharge curves of the HC/Na[FSA]–[C_3C_1pyrr][FSA] (x(Na[FSA]) = 0.20)/$NaCrO_2$ full cell at 333 K. Charge–discharge rate: 20 mA (g-$NaCrO_2$)$^{-1}$.

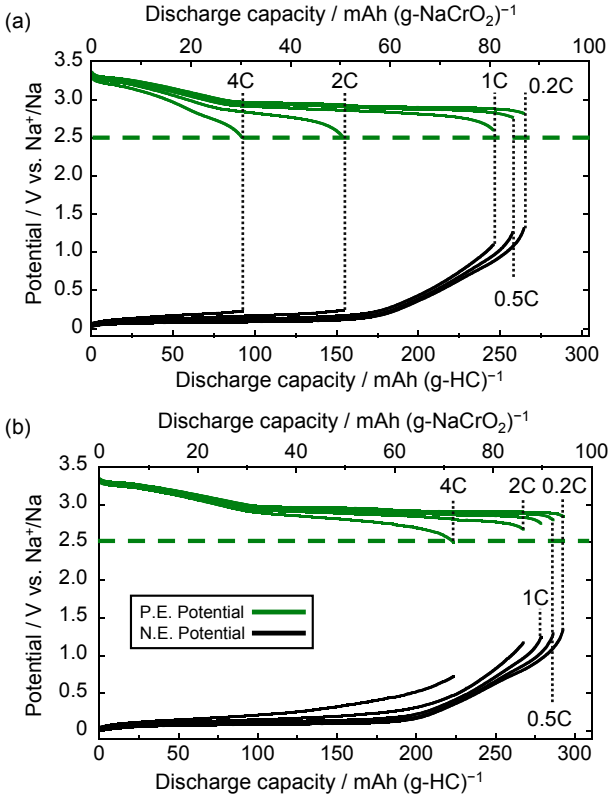

Figure 3. Discharge curves of the HC/Na[FSA]–[C_3C_1pyrr][FSA]/$NaCrO_2$ full cells at 333 K. Charge rate: 0.2 C rate. Discharge rates: 0.2–4 C rates (1 C = 100 mA (g-$NaCrO_2$)$^{-1}$). (a) Discharge curves for x(Na[FSA]) = 0.20. (b) Discharge curves for x(Na[FSA]) = 0.40.

For the electrolyte of x(Na[FSA]) = 0.40, the Na^+ ion depletion is suppressed compared with x(Na[FSA]) = 0.20, resulting in a higher discharge capacity. Thus, high Na^+ concentration electrolyte exhibited superior Na^+ supply capability.

3.2 Raman spectra of bulk electrolytes and analysis

Figure 4 shows the Raman spectra of the Na[FSA]–[C_3C_1pyrr][FSA] (x(Na[FSA]) = 0–0.50) ILs recorded at 333 K. The red circle plots and black lines represent the experimental spectra and fitting curves, respectively. The green, blue, and orange lines represent the deconvoluted components of free FSA^-, bound FSA^- ($[Na(FSA)_n]^{1-n}$), and $C_3C_1pyrr^+$, respectively. For neat [C_3C_1pyrr][FSA] IL (x(Na[FSA]) = 0), a band at 725 cm^{-1} attributed to the ν_s(N–S) vibration of free FSA^- anions was dominant. Upon the addition of Na[FSA] salt, a new band appeared at approximately 743 cm^{-1}, which is attributed to $[Na(FSA)_n]^{1-n}$ (n = 2–3).[22] The Raman peak shifts from 725 to 743 cm^{-1} as the Na[FSA] content increases, indicating a decrease in the amount of free FSA^- and an increase in the amount of bound FSA^- ($[Na(FSA)_n]^{1-n}$) in the IL. Thus, there is a correlation between the Na^+ concentration in the IL and the Raman shift. In the present study, we assume the formation of only mononuclear metal complex ions, i.e., the absence of multinuclear metal complex ions (aggregate form). This is because the ILs with Na salt fractions below 0.50 (x(Na[FSA]) ≤ 0.50) corresponds to the concentration region of $c_{Na^+} \leq 3.0$ mol dm^{-3}, indicating that they are not categorized in superconcentrated electrolytes (>3 or 4 mol dm^{-3}).[34,35] Moreover, Na[FSA] single salt, which is an ultimately concentrated electrolyte, shows a strong Raman band of ν_s(N–S) vibration located in the region around 750–760 cm^{-1}.[17] However, such a strong band is not observed for the IL even at x(Na[FSA]) = 0.50.

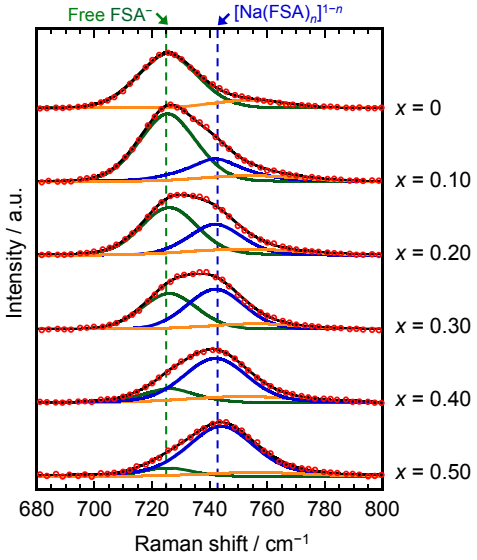

Figure 4. Raman spectra of the Na[FSA]–[C_3C_1pyrr][FSA] ILs (xNa[FSA]) = 0–0.50) measured at 333 K. The red circle plots and black lines represent the experimental spectra and fitting curves, respectively. The deconvoluted components of free FSA^-, bound FSA^- ($[Na(FSA)_n]^{1-n}$), and $C_3C_1pyrr^+$ are shown in green, blue, and orange, respectively.

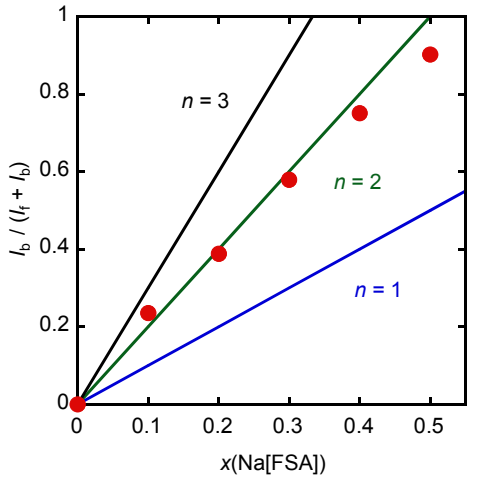

Figure 5. Correlation of integrated intensities of bound FSA^- Raman bands, as a function of x(Na[FSA]) at 333 K. Solid lines correspond to the states of $n = 1$, 2, and 3. The variable "n" represents the number of FSA^- anions coordinating with Na^+ ions in the complex $[Na(FSA)_n]^{1-n}$.

Figure 5 shows the ratio of the integrated Raman band intensity of the bound FSA^- (I_b) to that of the entire FSA^-, that is, the sum of bound FSA^- and free FSA^- (I_f), as a function of x(Na[FSA]). Assuming that the Raman scattering coefficients are identical for the free FSA^- and bound FSA^- in complex ions, the integrated intensity ratio of the bound FSA^- band to the entire FSA^- bands corresponds to the existence ratio of bound FSA^- over total FSA^- anions. Thus, the number of FSA^- anions coordinating with Na^+ ions (n) is indicated by the integrated intensity ratio vs. x(Na[FSA]) plots. The solid lines corresponding to $n = 1$, 2, and 3 are for visual guidance. While the obtained plots move slightly from a higher n region ($2 \leq n \leq 3$) to a lower n region ($1 \leq n \leq 2$) as the x(Na[FSA]) value increases from 0.10 to 0.50, these plots lie near the $n = 2$ line, indicating that the existence state of complex ions nearly equals $[Na(FSA)_2]^-$.

To ensure the validity of the obtained n value, we applied another calculation method without the assumption of the identical Raman scattering coefficients between free FSA^- and bound FSA^- (See Supporting Information). As shown in Fig. S3, the n value corresponds to x-intercept and is calculated to be 2.11, which is almost consistent with the above results (Fig. 5). Thus, assuming the bidentate coordination of FSA^- anion, the coordination number is four. On the other hand, it is well known that the coordination number of Na^+ has been reported to be approximately six in various electrolytes.[36–38] In TFSA-based IL electrolytes of Na^+ concentrations below 0.7 mol dm^{-3}, three $TFSA^-$ anions bidentately coordinate with one Na^+ ion, commensurate with the coordination number of six.[36] However, there are few reports on quantitative experimental studies for concentrated regions more than 1 mol dm^{-3}. Furthermore, several previous studies have revealed that some combinations of salts and solvents exhibit the coordination number around or less than five.[39–41]

3.3 In-situ Raman spectroscopy of Na/$NaCrO_2$ half-cell

The rate capability tests of the HC/$NaCrO_2$ full cell (Fig. 3) indicated that the positive electrode reaction was the rate-determining step of full-cell operation, which was largely dependent on the Na^+ ion concentration in the IL electrolyte. To further investigate the behavior of the positive electrode during discharging, Na/$NaCrO_2$ three-electrode cells with Na metal reference electrode were constructed for in-situ Raman spectroscopic analysis of the electrode/electrolyte interface. Figure S4 presents a schematic drawing of the interior and surface of the electrode. The positive electrode is a porous composite electrode that allows the electrolyte to permeate internally. Raman spectra are obtained by focusing the laser on the positive electrode surface (inside the red rectangular area) to check if the signals from $NaCrO_2$, AB, and the electrolyte are detected simultaneously (Fig. S5). Later, we discuss the phenomenon observed in rate capability tests according to the in-situ Raman results which represent the liquid structural change of the electrolyte in the black rectangular area in Fig. S4.

Figures 6 and 7 show the charge–discharge curves and Raman spectra obtained during the discharge process of the Na/$NaCrO_2$ half-cells for in-situ Raman spectroscopy with an electrolyte composition of x(Na[FSA]) = 0.20 and 0.40 at 333 K. For x(Na[FSA]) = 0.20 (Fig. 6a), a discharge capacity of 96 mAh $(g\text{-}NaCrO_2)^{-1}$ is achieved at 0.5 C-rate discharge; however, a discharge capacity of only 40 mAh $(g\text{-}NaCrO_2)^{-1}$ is observed at 4 C-rate discharge. As the discharge proceeds at both 0.5 C and 4 C rates, the Raman spectra undergo a red shift, reaching approximately 725 cm^{-1}, which corresponds to the free FSA^- state at the end of discharge. In particular, an increased polarization is observed before full utilization of the active material at the 4 C rate, which is attributed to the depletion of Na^+ ions in the vicinity of the electrode/electrolyte interface. In contrast, for x(Na[FSA]) = 0.40 (Fig. 7a), a discharge capacity of 103 mAh $(g\text{-}NaCrO_2)^{-1}$ is achieved at 0.5 C-rate discharge, and a discharge capacity of 82 mAh $(g\text{-}NaCrO_2)^{-1}$ is observed at 4 C-rate discharge. The Raman band exhibits a slight negative shift, reaching approximately 739 cm^{-1} at the end of discharge at both the 0.5 C and 4 C rates. However, the Raman shift during discharging is rather small even at the 4 C rate compared with the case of x(Na[FSA]) = 0.20, which is consistent with the obtained discharge capacity and higher utilization ratio of the active material. Thus, it is evident that Na^+ concentration polarization is suppressed for the electrolyte with x(Na[FSA]) = 0.40, which causes almost no depletion of Na^+ ions at the interface.

The phenomenon of improved rate capability is schematically depicted in Fig. 8. When a low Na^+ concentration electrolyte is used

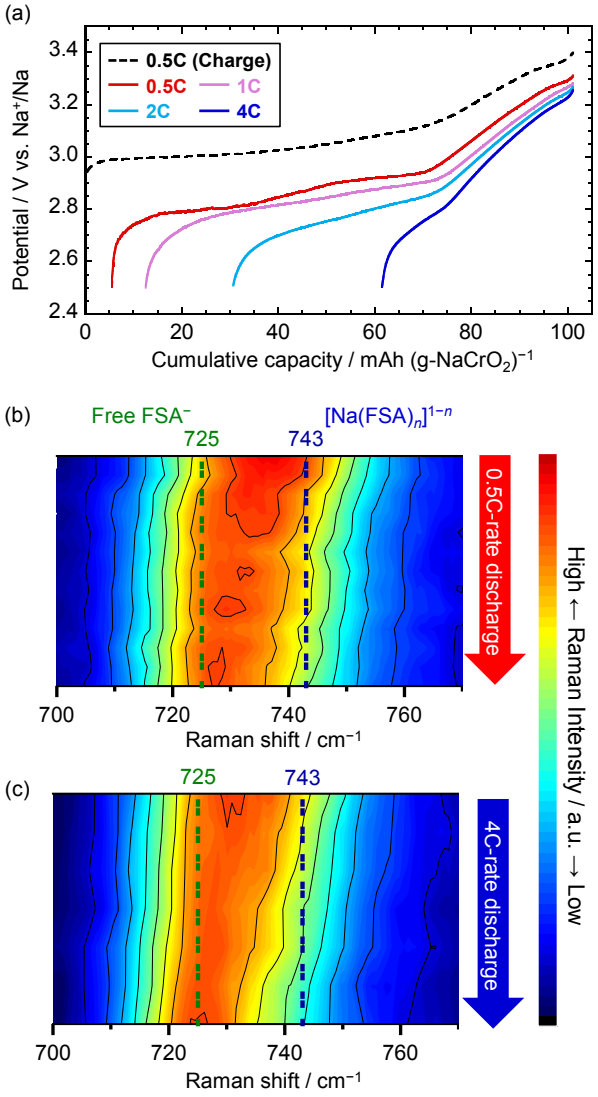

Figure 6. (a) Charge–discharge curves of the Na/Na[FSA]–$[C_3C_1pyrr][FSA]$ (x(Na[FSA]) = 0.20)/$NaCrO_2$ half-cell for in-situ Raman spectroscopy at 333 K. The broken line represents charge curve at the fixed rate of 0.5 C (1 C rate = 100 mA $(g\text{-}NaCrO_2)^{-1}$). The solid lines represent discharge curves at the rates of 0.5–4 C. (b, c) Contour maps of in-situ Raman intensity obtained during 0.5 C-rate and 4 C-rate discharge, respectively.

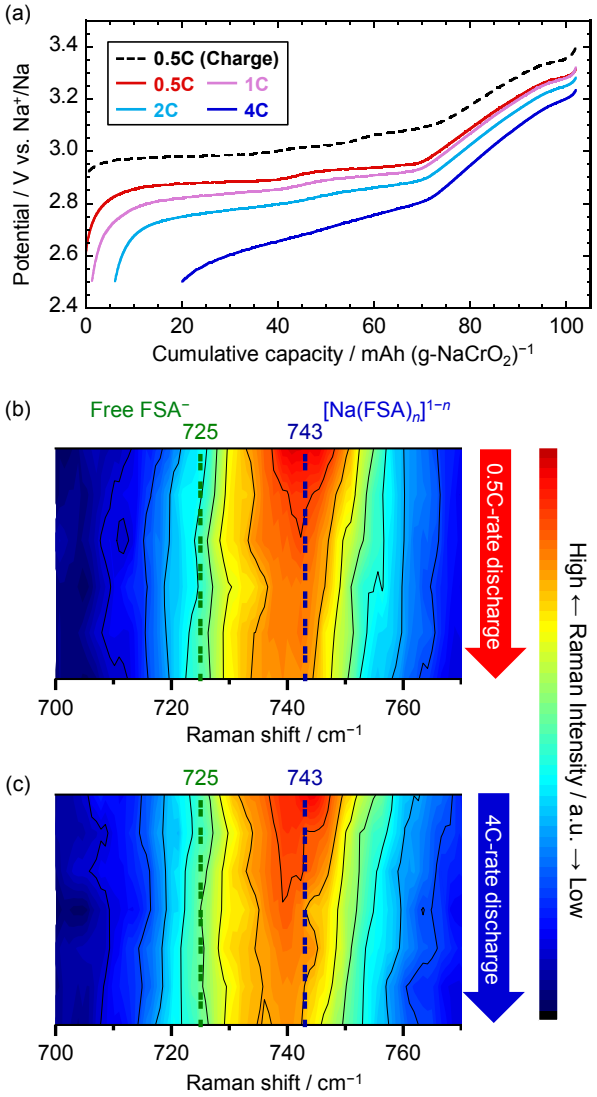

Figure 7. (a) Charge–discharge curves of the Na/Na[FSA]–$[C_3C_1pyrr][FSA]$ (x(Na[FSA]) = 0.40)/$NaCrO_2$ half-cell for in-situ Raman spectroscopy at 333 K. The broken line represents charge curve at the fixed rate of 0.5 C (1 C rate = 100 mA $(g\text{-}NaCrO_2)^{-1}$). The solid lines represent discharge curves at the rates of 0.5–4 C. (b, c) Contour maps of in-situ Raman intensity obtained during 0.5 C-rate and 4 C-rate discharge, respectively.

(Fig. 8a), an amount of Na^+ ions identical to that in the bulk electrolyte is present at the beginning of the discharge. As the discharge progresses, the concentration of Na^+ ions rapidly decreases, leading to depletion at the end of the discharge. However, in the case of a high Na^+ concentration electrolyte (Fig. 8b), a certain level of Na^+ concentration is maintained in the composite electrode even after the end of discharge, which is sufficient for a high utilization ratio of the active material. Thus, we confirmed that the IL electrolyte with a higher Na^+ concentration suppresses Na^+ depletion at the electrode/electrolyte interface and confers a superior rate capability to the positive electrode, overcoming the low ionic conductivity of the bulk electrolyte.

4. Conclusions

We investigated the factors that improve the rate capability of NIBs using IL electrolytes with high Na^+ concentrations. The results of HC/$NaCrO_2$ full-cell experiments suggested that the potential polarization of the positive electrode was largely dependent on the Na^+ ion concentration. According to ex-situ Raman spectroscopy of the bulk Na[FSA]–$[C_3C_1pyrr][FSA]$ IL electrolytes, it was deduced that the complex ion composed of Na^+ and FSA^- exists as $[Na(FSA)_2]^-$ in a wide range of Na^+ ion concentrations (x(Na[FSA]) = 0.10–0.50) at 333 K. To further investigate the mechanism of the improved discharge rate capability, in-situ Raman spectroscopic analysis was performed in the vicinity of the electrode/electrolyte interface at 333 K. In the case of a low Na^+ concentration electrolyte with x(Na[FSA]) = 0.20, the Raman band associated with the $[Na(FSA)_2]^-$ complex ion almost disappeared at the end of discharge, indicating that the depletion of Na^+ ions occurred at the interface during discharging. In contrast, for a high Na^+ concentration electrolyte with x(Na[FSA]) = 0.40, the Na^+ ion concentration was maintained even at the end of discharge. Although IL electrolytes with higher Na^+ concentrations exhibit lower Na^+ ion conductivity in the bulk, they can suppress Na^+ ion depletion and overcome transport limitations, at least in the vicinity

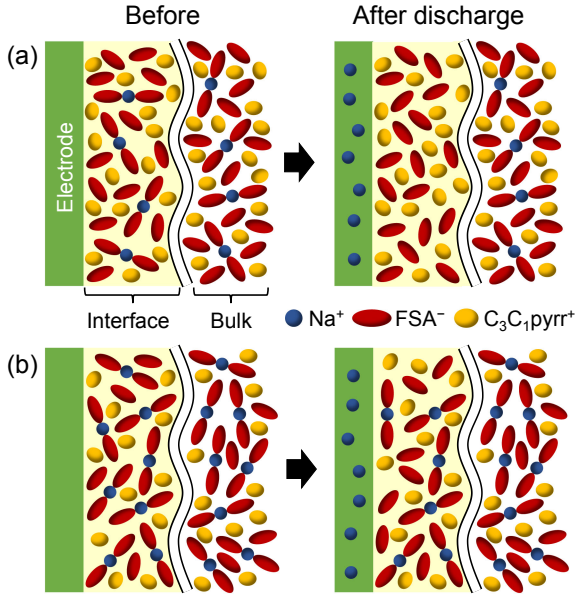

Figure 8. Schematic drawings of the positive electrode surface during discharge for the (a) low Na^+ concentration electrolyte and (b) high Na^+ concentration electrolyte.

of the electrode/electrolyte interface. In conclusion, ILs with concentrated Na^+ ions are beneficial for realizing high-power NIBs.

Acknowledgments

This study was partially supported by the Murata Science and Education Foundation, and ISHIZUE 2023 of Kyoto University. We thank Nippon Shokubai Co., Ltd. for supplying the Na[FSA] salt. We thank Kuraray Co., Ltd. for supplying the HC powder. We also thank Daicel Miraizu Ltd. for supplying the CMC powder.

CRediT Authorship Contribution Statement

Yoshifumi Ishio: Data curation (Equal), Investigation (Lead), Methodology (Equal), Validation (Equal), Visualization (Lead), Writing – original draft (Lead)
Takayuki Yamamoto: Conceptualization (Lead), Data curation (Equal), Funding acquisition (Lead), Methodology (Equal), Supervision (Equal), Validation (Equal), Writing – review & editing (Equal)
Koki Manabe: Data curation (Equal), Investigation (Equal), Methodology (Equal), Validation (Equal), Writing – review & editing (Supporting)
Toshiyuki Nohira: Data curation (Equal), Methodology (Equal), Supervision (Equal), Validation (Equal), Writing – review & editing (Equal)

Data Availability Statement

The data that support the findings of this study are openly available under the terms of the designated Creative Commons License in J-STAGE Data listed in D1 of References.

Conflict of Interest

The authors declare that they have no known competing financial interests.

References

D1. Y. Ishio, T. Yamamoto, K. Manabe, and T. Nohira, *J-STAGE Data*, https://doi.org/10.50892/data.electrochemistry.25255051, (2024).
1. *World Energy Outlook 2023*, IEA (2023). https://www.iea.org/reports/world-energy-outlook-2023 referred on Nov 25, 2023.
2. Z. Zhao, Y. Yuan, M. He, J. Jurasz, J. Wang, M. Egusquiza, E. Egusquiza, B. Xu, and D. Chen, *Renew. Energy*, **199**, 1482 (2022).
3. B. Dunn, H. Kamath, and J.-M. Tarascon, *Science*, **334**, 928 (2011).
4. T. M. Gür, *Energy Environ. Sci.*, **11**, 2696 (2018).
5. Y. Chen, Y. Kang, Y. Zhao, L. Wang, J. Liu, Y. Li, Z. Liang, X. He, X. Li, N. Tavajohi, and B. Li, *J. Energy Chem.*, **59**, 83 (2021).
6. K. Kubota, M. Dahbi, T. Hosaka, S. Kumakura, and S. Komaba, *Chem. Rec.*, **18**, 459 (2018).
7. *The Role of Critical Minerals in Clean Energy Transitions*, IEA (2021). https://www.iea.org/reports/the-role-of-critical-minerals-in-clean-energy-transitions referred on Nov 25, 2023.
8. M. I. Jamesh and A. S. Prakash, *J. Power Sources*, **378**, 268 (2018).
9. M. Watanabe, M. L. Thomas, S. Zhang, K. Ueno, T. Yasuda, and K. Dokko, *Chem. Rev.*, **117**, 7190 (2017).
10. T. Yamamoto, *Electrochemistry*, **90**, 101005 (2022).
11. T. Yamamoto and T. Nohira, *Chem. Rec.*, **23**, e202300169 (2023).
12. R. S. Carmichael, *Practical Handbook of Physical Properties of Rocks and Minerals (1988)* (1st ed.), CRC Press (1989).
13. M. S. Quinby-Hunt and K. K. Turekian, *Eos*, **64**, 130 (1983).
14. N. Yabuuchi, K. Kubota, M. Dahbi, and S. Komaba, *Chem. Rev.*, **114**, 11636 (2014).
15. J. Y. Hwang, S.-T. Myung, and Y. K. Sun, *Chem. Soc. Rev.*, **46**, 3529 (2017).
16. T. Nohira, T. Ishibashi, and R. Hagiwara, *J. Power Sources*, **205**, 506 (2012).
17. K. Matsumoto, T. Oka, T. Nohira, and R. Hagiwara, *Inorg. Chem.*, **52**, 568 (2013).
18. J. Serra Moreno, G. Maresca, S. Panero, B. Scrosati, and G. B. Appetecchi, *Electrochem. Commun.*, **43**, 1 (2014).
19. T. Carstens, A. Lahiri, N. Borisenko, and F. Endres, *J. Phys. Chem. C*, **120**, 14736 (2016).
20. C. V. Manohar, T. C. Mendes, M. Kar, D. Wang, C. Xiao, M. Forsyth, S. Mitra, and D. R. MacFarlane, *Chem. Commun.*, **54**, 3500 (2018).
21. K. Matsumoto, Y. Okamoto, T. Nohira, and R. Hagiwara, *J. Phys. Chem. C*, **119**, 7648 (2015).
22. C. Y. Chen, T. Kiko, T. Hosokawa, K. Matsumoto, T. Nohira, and R. Hagiwara, *J. Power Sources*, **332**, 51 (2016).
23. C. Ding, T. Nohira, K. Kuroda, R. Hagiwara, A. Fukunaga, S. Sakai, K. Nitta, and S. Inazawa, *J. Power Sources*, **238**, 296 (2013).
24. C. Y. Chen, K. Matsumoto, T. Nohira, C. Ding, T. Yamamoto, and R. Hagiwara, *Electrochim. Acta*, **133**, 583 (2014).
25. T. Yamamoto, T. Yamaguchi, T. Nohira, R. Hagiwara, A. Fukunaga, S. Sakai, and K. Nitta, *Electrochemistry*, **85**, 391 (2017).
26. A. Fukunaga, T. Nohira, R. Hagiwara, K. Numata, E. Itani, S. Sakai, and K. Nitta, *J. Appl. Electrochem.*, **46**, 487 (2016).
27. Y. Zheng, S. Jitto, J. Hwang, K. Matsumoto, and R. Hagiwara, *ACS Appl. Energy Mater.*, **5**, 14361 (2022).
28. Y. Marcus, *Pure Appl. Chem.*, **57**, 1129 (1985).
29. T. Yamamoto, K. Matsumoto, R. Hagiwara, and T. Nohira, *J. Phys. Chem. C*, **121**, 18450 (2017).
30. T. Yamamoto, K. Mitsuhashi, K. Matsumoto, R. Hagiwara, A. Fukunaga, S. Sakai, K. Nitta, and T. Nohira, *Electrochemistry*, **87**, 175 (2019).
31. K. Hiraoka and S. Seki, *J. Phys. Chem. C*, **127**, 11864 (2023).
32. M. Castriota, T. Caruso, R. G. Agostino, and E. Cazzanelli, *J. Phys. Chem. A*, **109**, 92 (2005).
33. Q. Huang, Y. Y. Lee, and B. Gurkan, *Ind. Eng. Chem. Res.*, **58**, 22587 (2019).
34. Y. Yamada, K. Furukawa, K. Sodeyama, K. Kikuchi, M. Yaegashi, Y. Tateyama, and A. Yamada, *J. Am. Chem. Soc.*, **136**, 5039 (2014).
35. Y. Yamada and A. Yamada, *J. Electrochem. Soc.*, **162**, A2406 (2015).
36. Y. Umebayashi, T. Yamaguchi, S. Fukuda, T. Mitsugi, M. Takeuchi, K. Fujii, and S. Ishiguro, *Anal. Sci.*, **24**, 1297 (2008).
37. K. Sadakane, K. Fujii, S. Tsuzuki, H. Watanabe, and Y. Umebayashi, *J. Mol. Liq.*, **248**, 53 (2017).
38. M. Galib, M. D. Baer, L. B. Skinner, C. J. Mundy, T. Huthwelker, G. K. Schenter, C. J. Benmore, N. Govind, and J. L. Fulton, *J. Chem. Phys.*, **146**, 084504 (2017).
39. S. K. Pattanayak and S. Chowdhuri, *J. Mol. Liq.*, **172**, 102 (2012).
40. Y. Zhou, S. Higa, C. Fang, Y. Fang, W. Zhang, and T. Yamaguchi, *Phys. Chem. Chem. Phys.*, **19**, 27878 (2017).
41. Y. Zhou, T. Yamaguchi, K. Yoshida, C. Fang, Y. Fang, and F. Zhu, *J. Mol. Liq.*, **274**, 173 (2019).